Supporting Information (SI) Appendix

Insights into proton-coupled electron transfer mechanisms of electrocatalytic H_2 oxidation and production

Samantha Horvath, Laura E. Fernandez, Alexander V. Soudackov, and Sharon Hammes-Schiffer*

Department of Chemistry, 104 Chemistry Building, Pennsylvania State University, University Park, PA 16802.

Table of Contents **Page**

COMPUTATIONAL DETAILS

A. Electronic structure calculations

The geometry optimizations and proton potentials were calculated using density functional theory in conjunction with the B3P86 density functional (1, 2) and the Stuttgart (SDD) pseudopotential for the Ni center (3), the 6-31G** basis set (4) for the transferring hydrogen, and the 6-31G* basis set (5, 6) for all other atoms. These calculations were performed with Gaussian 09 (7).

B. Approach 1: Using average structures

(i) Generating average structures

In Approach 1, we used average structures generated by averaging the optimized (1*a*) and (2*b*) structures to calculate both the anodic and the cathodic rate constants, and the anodic and cathodic probability distribution functions were assumed to be the same [i.e., $P_{\mathrm{a}}(R) \equiv P_{\mathrm{c}}(R)$]. The physical motivation for this approach is that the electron is expected to transfer between the complex and the electrode when thermal fluctuations of the complex lead to a structure that is in between the equilibrium reduced and oxidized structures. This approach is consistent with Marcus theory and the golden rule formulation, in which the nonadiabatic transition occurs at the crossing point between the initial and final states.

To obtain the average structures at the four Ni–N distances (2.94, 3.04, 3.14, and 3.25 Å), we performed a series of geometry optimizations for the (1*a*) and (2*b*) species with the Ni–N distance constrained to these values. The structures obtained from these constrained optimizations were then averaged together using the following procedure. For each Ni–N distance, the (1*a*) and (2*b*) structures were translated so that Ni was at the origin and rotated so

that the N atom involved in the proton transfer was along the negative *z*-axis. Subsequently, the root-mean-square deviation (RMSD) between the two structures was minimized with respect to the angle of the rigid structures about the *z*-axis. The resulting Cartesian coordinates of the (1*a*) and (2*b*) structures were averaged together to generate an average structure at this Ni–N distance.

(ii) Generating proton potentials

To generate proton potentials for the four different Ni–N distances, we began with the four average structures described above. For each average structure, the position of the transferring H was optimized for the reduced state (with H on Ni) and the oxidized state (with H on N), while all other atoms remained fixed. The hydrogen positions obtained from these constrained optimizations were used to define the proton axis for each Ni–N distance by connecting the optimized hydrogen positions for the reduced and oxidized states, as shown in Figure 3 of the main text. The proton potentials were generated on a one-dimensional grid along this axis for each Ni–N distance. Specifically, the hydrogen was moved along a grid of 24 points spanning this axis, and a single point DFT calculation with a convergence criterion of 10^{-8} a.u. was performed for each hydrogen position. These energies were then interpolated to create a grid of 1024 points using a cubic spline interpolation scheme (8). The sets of proton potentials generated for Ni–N distances of 2.94, 3.04, 3.14, and 3.25 Å are shown in Figure 3 of the main text.

(iii) Determining $P(R)$ and $k(R)$ for use in k_a and k_c

The Boltzmann probability for sampling different Ni–N distances is given by $P(R)$. For the calculations presented in this paper, we used the classical harmonic probability distribution function of the form:

$$P(R) = \frac{\exp[-k_{\text{eff}}(R-\bar{R})^2/(2k_{\text{B}}T)]}{\int_{-\infty}^{\infty} \exp[-k_{\text{eff}}(R-\bar{R})^2/(2k_{\text{B}}T)]dR}. \quad \text{(S1)}$$

In Approach 1, we assumed that $P_{\text{a}}(R) \equiv P_{\text{c}}(R)$ and chose $\bar{R}$ to be the average Ni–N distance of 3.25 Å (i.e., the average between the Ni–N distances for the optimized (1*a*) and (2*b*) structures).

The effective force constants, k_{eff}, were obtained for the optimized (1*a*) and (2*b*) structures by expressing the deviation δR of the proton donor-acceptor distance R from its equilibrium value $\bar{R}$ as a linear combination of normal mode coordinates. The expansion coefficients c_i were determined by projecting the normal mode vectors onto the proton donor-acceptor (i.e., Ni–N) axis. Assuming the classical harmonic oscillator form, evaluation of the time correlation function of the deviation δR leads to an expression for the effective force constant k_{eff} that includes contributions from all normal modes (9):

$$k_{\text{eff}} = \left[\sum_{i=1}^{3N} \frac{c_i^2}{k_i}\right]^{-1}, \quad \text{(S2)}$$

where the summation is over all normal modes with force constants k_i. This effective force constant corresponds to the second derivative of the electronic energy curve calculated by displacing the proton donor-acceptor distance from equilibrium and performing a constrained geometry optimization, where the displaced proton donor-acceptor distance is fixed. In other words, this effective force constant corresponds to the harmonic probability distribution function along R for which all other degrees of freedom respond instantaneously to changes in R. For the systems studied here, k_{eff} has values of 0.026409 and 0.020581 a.u. for the optimized (1*a*) and (2*b*) structures, respectively. In Approach 1, we used the average of these values, $k_{\text{eff}} = 0.023495$ a.u.

We performed the integration over R given in Eq. (5) numerically using a linear interpolation and extrapolation scheme for $k^{\mathrm{EPT}}(\eta;R)$ based on the values at the four Ni–N distances. We also performed these calculations by fitting $k^{\mathrm{EPT}}(\eta;R)$ to a Gaussian of the form $A_0 e^{-bR_{\mathrm{NiN}}^2}$ or to an exponential function of the form $A_0 e^{-bR_{\mathrm{NiN}}}$. The rate constants $k^{\mathrm{EPT}}(\eta)$ were qualitatively similar for these various approaches, as shown in Table S1 and Figure S1.

(iv) Tafel plot of k^{ET} vs k^{EPT}

As mentioned in the main text, the anodic EPT rate constant in Figure 5 exhibits slightly unusual curvature in the region $0.4 < \eta < 0.7$ V. This behavior is observed because the contributions from the various pairs of vibrational states depend on the overpotential. Analyses of the main contributions to the anodic and cathodic rate constants for various values of η are given in Tables S2 and S3.

As shown in Table S2, the main contributions at η = 0 V are from the relatively delocalized second and third excited reactant vibrational states with the localized ground product state. At η = 0.75 V, the main contribution is from the localized ground reactant state and the third excited product state, which is also localized on the same side. At η = 0.40 V, all three pairs of states contribute to the anodic rate constant. As shown in Table S3, this trend is not exhibited by the cathodic rate constant. These trends are also exhibited for $k_{\mathrm{a}}^{\mathrm{EPT}}(\eta)$ when a Gaussian or exponential fit of $k_{\mathrm{a}}^{\mathrm{EPT}}(\eta;R)$ is used, as illustrated in Figure S1, which indicates that the unusual curvature of $k_{\mathrm{a}}^{\mathrm{EPT}}(\eta)$ is much more dramatic for the Gaussian and exponential fits than for the linear fit of $k_{\mathrm{a}}^{\mathrm{EPT}}(\eta;R)$.

C. Approach 2: Using reduced and oxidized structures for anodic and cathodic rate constants, respectively

In Approach 2, the reduced and oxidized state structures are used to calculate the anodic and cathodic rate constants, respectively, and the anodic and cathodic probability distribution functions are different [i.e., $P_a(R) \neq P_c(R)$]. The physical motivation for this approach is that the structure of the complex is expected to be closer to the equilibrium reduced state structure for the anodic process and closer to the equilibrium oxidized state structure for the cathodic process. In this approach, the structure is assumed to respond to the addition or removal of an electron faster than the timescale of the electrochemistry. This perspective differs from Approach 1, which assumes that the electron transfer occurs only when thermal fluctuations result in a structure that is the average of the equilibrium reduced and oxidized state structures. The practical advantage of Approach 2 is that it avoids the averaging procedure, which could introduce non-physical angles and bond lengths. As shown below, the two approaches give qualitatively similar results, although some differences were observed. Further calculations and comparisons to experiment are required to determine which approach is preferable.

We used the optimized equilibrium (1*a*) and (2*b*) geometries, corresponding to Ni–N distances of 3.31 Å and 3.20 Å, respectively, as well as the geometries generated by performing a series of optimizations for the (1*a*) and (2*b*) species with the Ni–N distance constrained to the values of 2.94, 3.04, 3.14, and 3.25 Å. Thus, we obtained a set of reduced state structures from the (1*a*) optimizations and a set of oxidized state structures from the (2*b*) optimizations. For each set of structures, we determined the proton axes using a procedure similar to that used for Approach 1. Specifically, for each structure, we optimized the transferring H for the reduced state (with H on Ni) and the oxidized state (with H on N) with all other atoms fixed, and the

proton axis was generated by connecting these two optimized hydrogen positions, as depicted in Figure 3 in the main text. The proton potentials were generated by performing single point DFT calculations with a convergence criterion of 10^{-8} a.u. as the hydrogen was moved along a grid of 24 points spanning this axis and subsequently interpolating to create a grid of 1024 points. The proton potentials generated for the reduced and oxidized state structures are shown in Figure S2. Interestingly, for each Ni–N distance, the averages of the proton potentials for the optimized reduced and oxidized state structures used in Approach 2 are nearly identical to the proton potentials generated for the average reduced and oxidized state structures used in Approach 1. The comparison between the average of the reduced and oxidized state proton potentials used in Approach 2 and the proton potentials for the average structures used in Approach 1 is given in Figure S3.

As mentioned above, the anodic and cathodic probability functions, $P_{\mathrm{a}}(R)$ and $P_{\mathrm{c}}(R)$, are different in Approach 2. In this paper, these probability functions were chosen to be of the form given in Eq. (S1) with $\overline{R}$ and k_{eff} determined from the equilibrium (1*a*) and (2*b*) structures, respectively. Thus, $\overline{R} = 3.31$ Å and k_{eff} = 0.026409 a.u. for $P_{\mathrm{a}}(R)$, and $\overline{R} = 3.20$ Å and k_{eff} = 0.020581 a.u. for $P_{\mathrm{c}}(R)$. The anodic rate constant $k_{\mathrm{a}}^{\mathrm{EPT}}(\eta;R)$ was calculated with Eq. (3) using the proton potentials for the reduced state structures, and the overall anodic rate constant $k_{\mathrm{a}}^{\mathrm{EPT}}(\eta)$ was calculated using Eq. (5) and the probability distribution function $P_{\mathrm{a}}(R)$ with the same linear interpolation–extrapolation scheme for the numerical integration discussed above for Approach 1. The cathodic rate constant $k_{\mathrm{c}}^{\mathrm{EPT}}(\eta;R)$ was calculated with Eq. (4) using the proton potentials for the oxidized state structures, and the overall cathodic rate constant $k_{\mathrm{c}}^{\mathrm{EPT}}(\eta)$ was

calculated using Eq. (5) and the probability distribution function $P_c(R)$ with the same numerical integration procedure as for $k_a^{EPT}(\eta)$.

In this approach, the anodic and cathodic rate constants are not equal at η = 0 because different proton potentials and probability distribution functions are used. In this case, the standard rate constant can be determined by identifying the overpotential η_0 at which the anodic and cathodic rate constants are equal. Thus, we numerically determine the appropriate constant shift of the standard electrode potential to effectively account for differences in the total partition functions of the reduced and oxidized species. For this system, η_0 = 0.1236 V.

We performed similar analyses with Approach 2 as with Approach 1. The dominant distance was found to be R_{NiN} = 3.28 and 3.10 Å for the anodic and cathodic processes, respectively. An analysis of the main contributions to the standard rate constants, analogous to that in Table 1 and Figure 4 in the main text, is given in Tables S4 and S5 and Figure S4. The resulting Tafel plot that compares the ET and EPT rate constants, analogous to Figure 5 in the main text, is given in Figure S5. Note that the anodic EPT rate constant does not exhibit the behavior discussed in the main text because the dominant states remain consistent for the region of overpotential studied.

Table S1: Analysis of the dominant Ni–N distance and relative standard rate constants for three different fits of $k^{EPT}(\eta=0;R)$ using Approach 1.

type of fit	R_{dom} (Å)	k_s [b]
linear[a]	3.00	1.000
Gaussian	2.91	1.003
exponential	2.91	1.081

[a]Interpolation–extrapolation scheme used for $k^{EPT}(\eta;R)$ to generate data presented in Table 1 and Figure 5 of main text.

[b]Standard rate constants ($\eta = 0$) given relative to rate constant obtained with linear fit.

Table S2: Analysis of main contributions to the anodic rate constant at various values of η for Approach 1.

R_{dom} (Å) *	R (Å) *	η (V)	μ / ν †	P_μ ‡	$S^2_{\mu\nu}$ §	$e^{-\Delta G^\dagger_{\nu\mu}/k_BT}$ ¶	% contrib. ‖
3.00	3.04	0.0	2/0	3.8×10^{-6}	0.215	6.8×10^{-3}	42
			3/0	1.3×10^{-6}	0.571	9.8×10^{-3}	55
3.00	3.04	0.40	0/3	1.0	0.426	2.3×10^{-6}	39
			2/0	3.8×10^{-6}	0.215	3.5×10^{-1}	19
			3/0	1.3×10^{-6}	0.571	4.2×10^{-1}	21
3.23	3.25	0.75	0/3	1.0	0.855	3.4×10^{-4}	98
3.24	3.25	1.00	0/3	1.0	0.855	1.4×10^{-2}	98

* R_{dom} is the dominant Ni–N distance and R is the closest Ni–N distance for which proton potentials were obtained for the reduced complex.

† μ and ν correspond to the proton vibrational states for the reduced and oxidized states, respectively, of the catalyst.

‡ P_μ is the Boltzmann probability for state μ.

§ $S_{\mu\nu}$ is the overlap integral between the proton vibrational wavefunctions associated with states μ and ν.

¶ $\Delta G^\dagger_{\mu\nu}$ is the effective free barrier at the specified value of η and $\varepsilon = 0$.

‖ % contrib. is the percentage contribution to the overall rate constant at that distance R for the specified η, $k_a^{EPT}(\eta; R)$, including only contributions greater than 10%.

Table S3: Analysis of main contributions to the cathodic rate constant at various values of η for Approach 1.

R_{dom} (Å) *	R (Å) *	η (V)	μ / ν †	P_ν ‡	$S^2_{\mu\nu}$ §	$e^{-\Delta G^\dagger_{\nu\mu}/k_BT}$ ¶	% contrib. ‖
3.00	3.04	0.0	2/0	1.0	0.215	2.6×10^{-8}	42
			3/0	1.0	0.571	1.2×10^{-8}	55
3.09	3.14	– 0.40	3/0	1.0	0.867	1.8×10^{-5}	99
3.12	3.14	– 0.75	3/0	1.0	0.867	6.5×10^{-3}	98
3.13	3.14	– 1.00	3/0	1.0	0.867	1.1×10^{-1}	97

* R_{dom} is the dominant Ni–N distance and R is the closest Ni–N distance for which proton potentials were obtained for the reduced complex.

† μ and ν correspond to the proton vibrational states for the reduced and oxidized states, respectively, of the catalyst.

‡ P_ν is the Boltzmann probability for state ν.

§ $S_{\mu\nu}$ is the overlap integral between the proton vibrational wavefunctions associated with states μ and ν.

¶ $\Delta G^\dagger_{\mu\nu}$ is the effective free barrier at the specified value of η and $\varepsilon = 0$.

‖ % contrib. is the percentage contribution to the overall rate constant at that distance R for the specified η, $k_c^{EPT}(\eta; R)$, including only contributions greater than 10%.

Table S4: Analysis of main contributions to the anodic standard rate constant at a Ni–N distance close to the dominant distance and at the equilibrium Ni–N distance for Approach 2.

R (Å) *	μ / ν †	P_μ ‡	$S_{\mu\nu}^2$ §	$e^{-\Delta G_{\nu\mu}^\dagger / k_B T}$ ¶	% contrib. ‖
3.25	0/2	1.0	0.907	6.1×10^{-8}	99
3.31	0/2	1.0	0.918	5.1×10^{-8}	99

*The Ni–N distance of 3.25 Å is 0.03 Å shorter than the dominant distance, and the Ni–N distance of 3.31 Å is the equilibrium distance for the reduced complex.

†μ and ν correspond to the proton vibrational states for the reduced and oxidized states, respectively, of the catalyst.

‡P_μ is the Boltzmann probability for state μ.

§$S_{\mu\nu}$ is the overlap integral between the proton vibrational wavefunctions associated with states μ and ν.

¶$\Delta G_{\mu\nu}^\dagger$ is the effective free barrier at $\eta = \eta_0 = 0.1236$ V and $\varepsilon = 0$.

‖ % contrib. is the percentage contribution to the overall standard rate constant at that distance R, $k_a^{\mathrm{EPT}}(\eta = \eta_0; R)$, including only contributions greater than 10%.

Table S5: Analysis of main contributions to the cathodic standard rate constant at a Ni–N distance close to the dominant distance and at the equilibrium Ni–N distance for Approach 2.

R (Å) *	μ / ν †	P_ν ‡	$S_{\mu\nu}^2$ §	$e^{-\Delta G_{\nu\mu}^\dagger / k_B T}$ ¶	% contrib. ‖
3.14	1/0	1.0	0.887	4.6×10^{-8}	98
3.20	2/0	1.0	0.922	1.2×10^{-8}	100

*The Ni–N distance of 3.14 Å is 0.04 Å larger than the dominant distance, and the Ni–N distance of 3.20 Å is the equilibrium distance for the oxidized complex.

†μ and ν correspond to the proton vibrational states for the reduced and oxidized states, respectively, of the catalyst.

‡P_ν is the Boltzmann probability for state ν.

§$S_{\mu\nu}$ is the overlap integral between the proton vibrational wavefunctions associated with states μ and ν.

¶ $\Delta G_{\mu\nu}^\dagger$ is the effective free barrier at $\eta = \eta_0 = 0.1236$ V and $\varepsilon = 0$.

‖ % contrib. is the percentage contribution to the overall standard rate constant at that distance R, $k_c^{\mathrm{EPT}}\left(\eta = \eta_0; R\right)$, including only contributions greater than 10%.

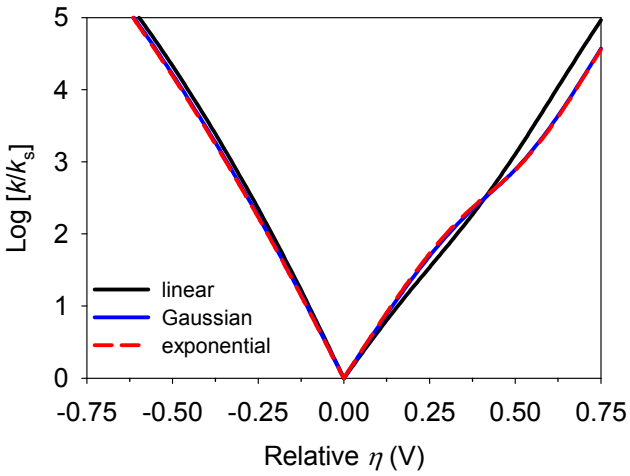

Figure S1: Electrochemical rate constants as functions of overpotential for the EPT reaction of interest generated using Approach 1 with three different fits of $k^{EPT}(\eta;R)$: linear, Gaussian, and exponential. The standard potential for the EPT reaction is chosen to be zero overpotential (η = 0).

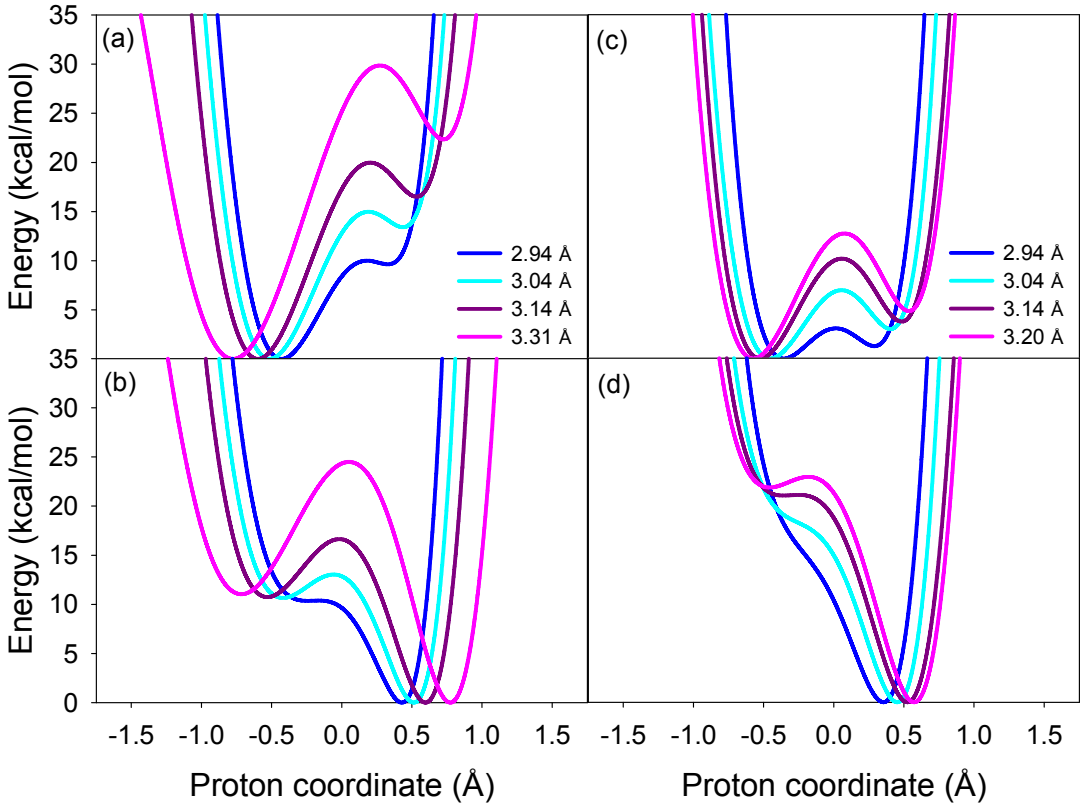

Figure S2: Proton potentials for the reduced and oxidized states of the anodic and cathodic processes using Approach 2. (a) & (b): reduced and oxidized states, respectively, of the anodic process at Ni–N distances of 2.94, 3.04, 3.14, and 3.31 Å; (c) & (d): reduced and oxidized states, respectively, of the cathodic process at Ni–N distances of 2.94, 3.04, 3.14, and 3.20 Å.

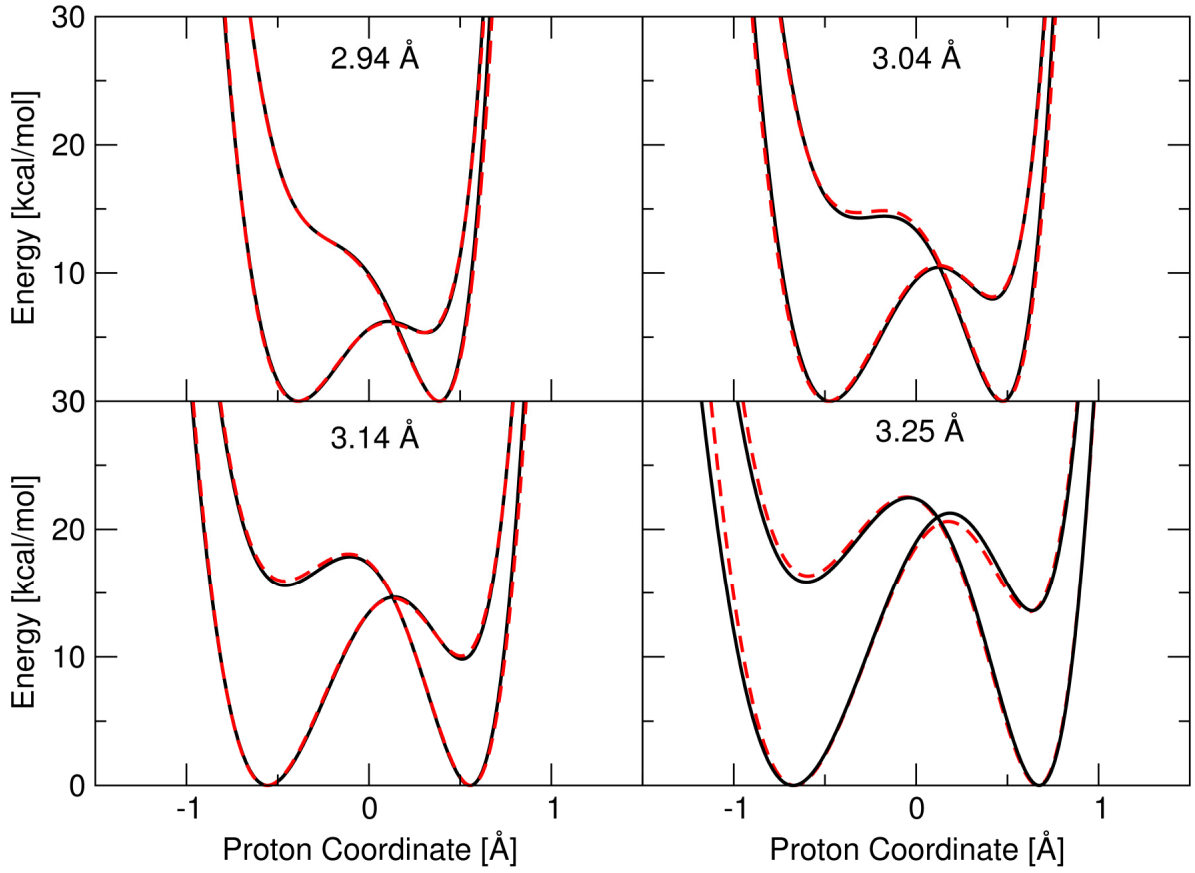

Figure S3: Comparison between the proton potentials generated in Approach 1 for the average geometries obtained by averaging the optimized reduced and oxidized state geometries (solid black lines) and the average of the proton potentials generated in Approach 2 for the optimized reduced and oxidized state geometries (dashed red lines). The results are given for geometries optimized with the Ni–N distance constrained to 2.94, 3.04, 3.14, and 3.25 Å, as indicated. The proton potential for the average reduced/oxidized state geometry and the average of the reduced and oxidized state proton potentials are in remarkable agreement.

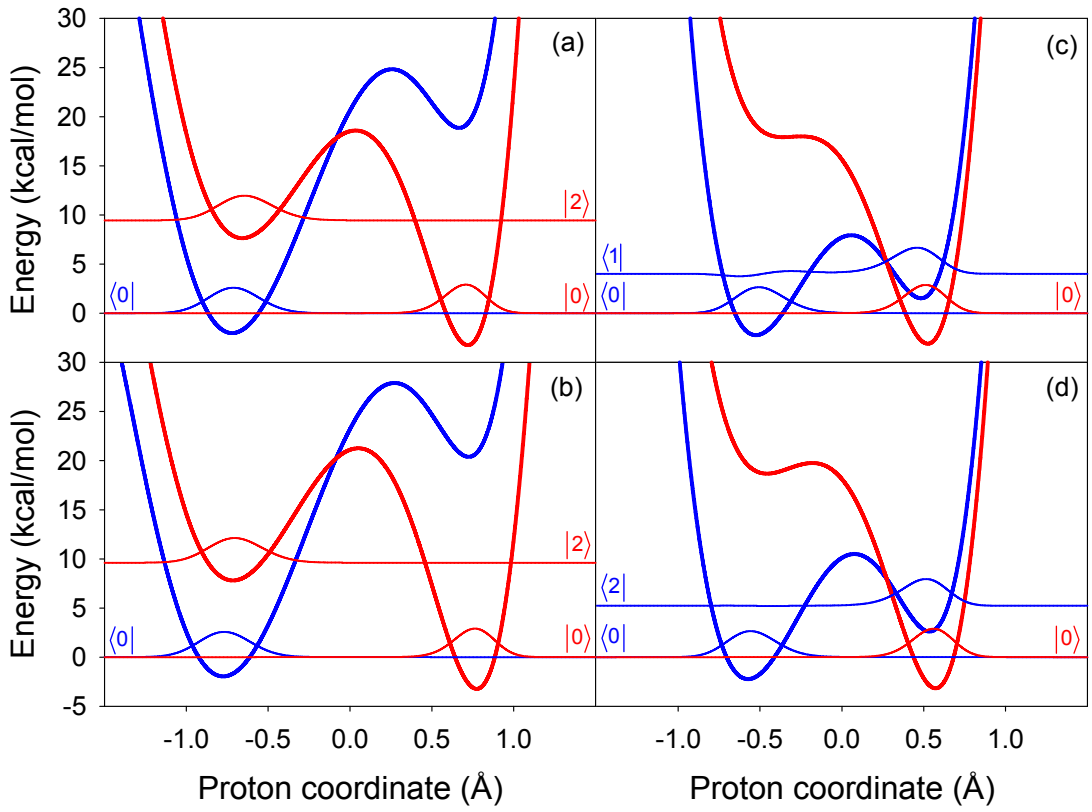

Figure S4: Proton potentials and corresponding vibrational wavefunctions for the contributing proton vibrational states (as given in Tables S4 and S5) for the reduced state (blue) and the oxidized state (red) for Approach 2. (a) & (b): anodic process at the nearly dominant Ni–N distance of 3.25 Å and the equilibrium Ni–N distance of 3.31 Å, respectively. (c) & (d): cathodic process at the nearly dominant Ni–N distance of 3.14 Å and the equilibrium Ni–N distance of 3.20 Å, respectively.

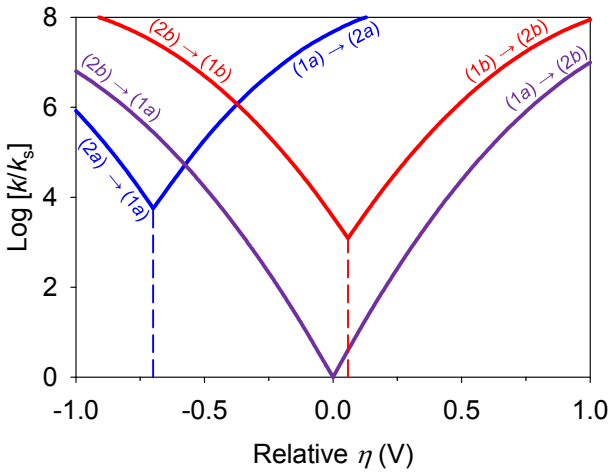

Figure S5: Electrochemical rate constants as functions of potential for the ET and EPT reactions of interest generated using Approach 2. The rate constants are given relative to k_s, the standard rate constant for the EPT reaction. The standard potential for the EPT reaction is chosen to be zero overpotential ($\eta = 0$), and the standard potentials for the ET reactions are shifted relative to this value by their relative reduction potentials. Thus, the overpotential η is defined to be the applied potential relative to the standard potential for the EPT reaction. The curves are labeled according to the specific ET and EPT reactions.

References:

1. Becke AD (1993) Density-functional thermochemistry. III. The role of exact exchange. *J. Chem. Phys.* 98:5648-5652.
2. Perdew JP (1986) Density-functional approximation for the correlation energy of the inhomogeneous electron gas. *Phys. Rev. B* 33:8822-8824.
3. Dolg M, Wedig U, Stoll H, & Preuss H (1987) Energy-adjusted ab initio pseudopotentials for the first row transition elements. *J. Chem. Phys.* 86:866-872.
4. Hariharan PC & Pople JA (1973) The Influence of Polarization Functions on Molecular Orbital Hydrogenation Energies. *Theoret. chim. Acta* 28:213-222.
5. Hehre WJ, Ditchfield R, & Pople JA (1972) Self-Consistent Molecular Orbital Methods. XII. Further Extensions of Gaussian-Type Basis Sets for Use in Molecular Orbital Studies of Organic Molecules. *J. Chem. Phys.* 56:2257-2261.
6. Francl MM*, et al.* (1982) Self-consistent molecular orbital methods. XXIII. A polarization-type basis set for second-row elements. *J. Chem. Phys.* 77:3654-3665.
7. Gaussian 09 Revision B.01; Frisch, M. J.; Trucks, G. W.; Schlegel, H. B.; Scuseria, G. E.; Robb, M. A.; Cheeseman, J. R.; Scalmani, G.; Barone, V.; Mennucci, B.; Petersson, G. A.; Nakatsuji, H.; Caricato, M.; Li, X.; Hratchian, H. P.; Izmaylov, A. F.; Bloino, J.; Zheng, G.; Sonnenberg, J. L.; Hada, M.; Ehara, M.; Toyota, K.; Fukuda, R.; Hasegawa, J.; Ishida, M.; Nakajima, T.; Honda, Y.; Kitao, O.; Nakai, H.; Vreven, T.; Montgomery, J., J. A.; Peralta, J. E.; Ogliaro, F.; Bearpark, M.; Heyd, J. J.; Brothers, E.; Kudin, K. N.; Staroverov, V. N.; Kobayashi, R.; Normand, J.; Raghavachari, K.; Rendell, A.; Burant, J. C.; Iyengar, S. S.; Tomasi, J.; Cossi, M.; Rega, N.; Millam, N. J.; Klene, M.; Knox, J. E.; Cross, J. B.; Bakken, V.; Adamo, C.; Jaramillo, J.; Gomperts, R.; Stratmann, R. E.; Yazyev, O.; Austin, A. J.; Cammi, R.; Pomelli, C.; Ochterski, J. W.; Martin, R. L.; Morokuma, K.; Zakrzewski, V. G.; Voth, G. A.; Salvador, P.; Dannenberg, J. J.; Dapprich, S.; Daniels, A. D.; Farkas, Ö.; Foresman, J. B.; Ortiz, J. V.; Cioslowski, J.; Fox, D. J. Gaussian 09, Revision B.01; Gaussian, Inc.: Wallingford, CT, 2010.
8. Press WH, Flannery BP, Teukolsky SA, & Vetterling WT (1989) *Numerical Recipes: The Art of Scientific Computing* (Cambridge University Press, New York).
9. Auer B, Fernandez LE, & Hammes-Schiffer S (2011) Theoretical Analysis of Proton Relays in Electrochemical Proton-Coupled Electron Transfer. *J. Am. Chem. Soc.* 133:8282-8292.